Solid Freeform Fabrication 2016: Proceedings of the 27th Annual International Solid Freeform Fabrication Symposium – An Additive Manufacturing Conference
Reviewed Paper

Three-dimensional finite element thermal analysis in selective laser melting of Al-Al_2O_3 powder

Quanquan Han, Rossitza Setchi, Sam L. Evans and Chunlei Qiu

School of Engineering, Cardiff University, Cardiff, CF24 3AA, UK

Abstract

The selective laser melting (SLM) of aluminium-based composites continues to be a challenge due to the high reflectivity, high thermal conductivity and oxidation of aluminium, all of which directly influence the thermal performance of each layer during SLM. Due to the extremely rapid melting and cooling rate of aluminium, however, it is difficult to measure thermal performance within practical SLM applications. A three-dimensional finite element simulation model is thus developed in this study to simulate the transient temperature distribution and molten pool dimensions of the premier layer during the SLM of Al-Al_2O_3 composite powder. In order to produce high-quality parts with minimum defects in a highly efficient manner, the predicted optimum volumetric energy density is found to be 40 J/mm^3, with laser power 300 W, scanning speed 1000 mm/s, hatch spacing 150 μm and layer thickness 50 μm; the molten pool size that is produced is 165 μm in length, 160 μm in width and 77 μm in depth, with a predicted maximum temperature of around 3400°C. All of these factors may contribute to the creation of good metallurgic bonding.

Introduction

One of the main advantages of selective laser melting (SLM) is that the technique provides an integrated way of manufacturing three-dimensional metallic components from computer-aided design files using a layer-by-layer principle [1]. It also shows potential in the fabrication of advanced engineering components in order to meet the demanding requirements of the aerospace, automotive and biomedical industries [2].

Due to its light weight, high specific strength and good corrosion resistance, aluminium is widely used in various domains, including within the automotive and aerospace industries [3]. Several studies have been conducted on the SLM of aluminium alloys [4]. In comparison with aluminium alloys, aluminium based composites exhibit better mechanical strength, wear resistance

and high temperature properties; the SLM of Al-Al_2O_3 nanocomposites is currently used in new applications within the automotive and aerospace industries [5]. The quality of the parts produced via SLM generally depends on the temperature distribution under various operating parameters, such as laser power, scanning speed, hatch spacing and scanning strategy [6]. In order to obtain the desired SLM components, further research is thus required to explore the relationship between process parameters and thermal behaviour during SLM [7]. It is difficult to measure thermal performance within practical SLM applications, however, due to the extremely rapid melting and cooling rate; researcher therefore consider numerical simulation to be a suitable approach for exploring these issues.

This paper explores the thermal behaviour within a scan of the premier layer's Al-Al_2O_3 nanocomposites through the numerical simulation approach. It is important to scan the premier layer, as doing so not only determines the subsequent layers' coating behaviour but also affects the dimensional accuracy and mechanical properties of the final parts. The properties of a part produced by this process therefore depend strongly on the quality of the premier layer, as that layer determines the nature and shape of the molten pool. Gaining an understanding of the thermal behaviour during the scanning of the premier layer is crucial for engineers in order to optimise the laser strategy and to improve component quality using SLM technology.

This paper thus has two objectives: first, to develop a three-dimensional finite element model for the scanning of the premier layer's Al-Al_2O_3 powder, and second, to employ different combinations of process parameters (such as laser power and scanning speed) to predict thermal behaviour and to explore the optimum volumetric energy density for fabricating high-quality components.

Related work

Researchers have employed finite element analysis (FEA), one of the most widely used numerical methods in use today, for temperature field analysis of various additive layer manufacturing processes. In early papers, Childs [8] investigated the influence of process parameters on the mass of melted single layers in SLM and found that an increase in scanning speed resulted in a larger melted mass. Matsumoto et al. [9] proposed a method for calculating the

distribution of temperature and stress in the SLM of single metallic layers; they found that the solid layer on the powder bed warped due to heating and cooling while the laser travelled on the track. When the neighbouring track began to solidify, large tensile stresses occurred at the side end of the solid part. Dai and Shaw [10] investigated the effect of the laser scanning strategy on residual stress and distortion and found that a scanning pattern with frequent 90° changes in the scanning direction at every turn could lead to a reduction of concave upwards and downwards distortions.

More recently, Hussein et al. [11] developed a transient finite element model for the analysis of temperature and stress fields in single layers built without support in SLM. They found that the predicted length of the molten pool increased at higher scanning speeds, while both the width and depth of the molten pool decreased. Li and Gu [12] analysed thermal behaviour during the SLM of aluminium alloy powders and obtained the optimum molten pool width (111.4 μm) and depth (67.5 μm) for a specific combination of parameters (laser power 250 W and scan speed 200 mm/s). Roberts et al. [13] employed an element birth-and-death strategy to analyse the 3D temperature field in multiple layers within a powder bed. Similar studies have explored the behaviour of other materials during SLM. For example, Kolossov et al. [14] proposed a 3D finite element model to predict the temperature distribution on the top surface of a titanium powder bed during the laser sintering process; their studies showed that changes in thermal conductivity determined the behaviour and development of thermal processes. In addition, Patil and Yadava [1] investigated the temperature distribution in a single metallic powder layer during metal laser sintering and found that temperature increased with increases in laser power and laser on-time, but decreased with increases in laser off-time and hatch spacing.

A basic heat transfer model consists primarily of a heat source module and a thermal physics module. The fibre laser (Nd: YAG, λ=1.06 μm) employed in the SLM process normally operates in continuous-wave mode. The heat flux *I(r)* follows a Gaussian distribution and can be expressed as [11]:

$$I(r) = \frac{2AP}{\pi {r_0}^2} \exp(-\frac{2r^2}{{r_0}^2}) \qquad (1)$$

where A is absorptivity, P and r are laser power and radial distance from the laser centre, respectively, and r_0 denotes the laser spot radius.

The absorptivity of a composite powder containing *n* components can be calculated using the following equation [15]:

$$A = \sum_{i=1}^{n} A_i \gamma_i \qquad (2)$$

where A_i and γ_i denote the absorptivity and volume fraction of a component, respectively. Tolochko et al. [15] measured the absorptivity of Al_2O_3 powder to be 3% under a pulsed Nd-YAG laser (λ=1.06μm pulse duration of 5ms, repetition rate up to 20Hz, energy content per pulse up to 20J) . In the present work, the nanocomposite powder was composed of 96 vol.% Al and 4 vol.% Al_2O_3 powder. Before the laser melting process, the employed aluminium plate was preheated to 150°C (423K) to reduce the thermal distortion of the final parts; thus, considering the porosity of the powder bed, the temperature of the powder bed could be around 90°C. The corresponding absorptivity of Al was around 12%, which can be seen from Figure 1 [16]. The absorptivity of the Al-Al_2O_3 composite powder may then be determined using Eq. (2), yielding an absorptivity figure of 11.6%.

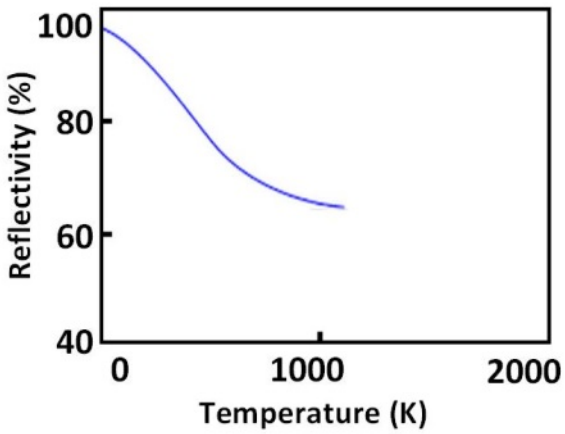

Figure 1. Reflectivity of Al at 1.06 μm radiation [16].

The porosity of the powder bed is crucial in SLM, as it affects both the thermal conductivity of the powder in the laser melting stage and the porosity of the final parts. Aboulkhair et al. [17] determined that the pores of the final parts can be categorised as metallurgical pores and keyhole pores. Metallurgical pores are spherically shaped and small in size (less than 100 μm); they are created at slow scanning speeds from gases trapped within the melt pool or are evolved from the powder during consolidation. These interstitial gases derive from the high porosity of the powder bed. Keyhole pores, in contrast, are irregularly shaped and large in size (greater than 100 μm),

which can be attributed to the rapid solidification of the metal without the complete filling of gaps with molten metal. Oxidation-caused pores can be classified as keyhole pores, because when a thin film meets another film, few non-melted powders will be trapped. The content of the metallurgical pores also decreases with an increase in the scanning speed, while keyhole pores increase as the scanning speed exceeds a critical speed. In general, the formation of metallurgical pores can be partially attributed to the powder bed porosity (φ) and can be expressed as [12]:

$$\varphi = 1 - \frac{\rho_p}{\rho_b} \qquad (3)$$

where ρ_p and ρ_b represent the density of powder and bulk materials, respectively. The density of the bulk composite material can be calculated using the following equation:

$$\rho_b = \sum_{i=1}^{n} \rho_i \gamma_i \qquad (4)$$

Where ρ_i and γ_i denote the density and volume, respectively, of component *i*. The density ρ_b of 2.75 g/cm^3 is found when the composite powder comprises 96 vol.% Al and 4 vol.% Al_2O_3. The density of the powder ρ_p can be evaluated by the apparent density, which is roughly 1.65 g/cm^3. Thus, the porosity of the powder bed is calculated to be 40%, which is in agreement with the findings of Dong et al. [18], who suggested that the porosity can evolve from 50% (initial powder bed) to the minimum value of 0 (fully dense material) during the laser sintering process.

Using a thermal physics module is necessary because SLM involves a phase-change process; this type of thermal analysis is thus a nonlinear transient analysis and a number of thermophysical properties should be determined for the ANSYS simulation. In order to analyse the phase transformation, the latent heat should be considered: this represents the heat energy that the system stores or releases during a phase change. To account for latent heat, the enthalpy of the material *H* as a function of the temperature is defined: it is the integral of material density p times specific heat $c(T)$ with respect to temperature *T*:

$$H = \int pc(T)dT \qquad (5)$$

Other thermophysical properties to consider include the density and thermal conductivity of the aluminium powder bed, which can be expressed as [19]:

$$k_p = k_b(1 - \varphi) \qquad (6)$$

where k_p and k_b denote the thermal conductivity of the powder bed and bulk materials, respectively; φ is the porosity of the powder bed. Typical solid thermophysical properties of aluminium and alumina are shown in Figure 2 [19].

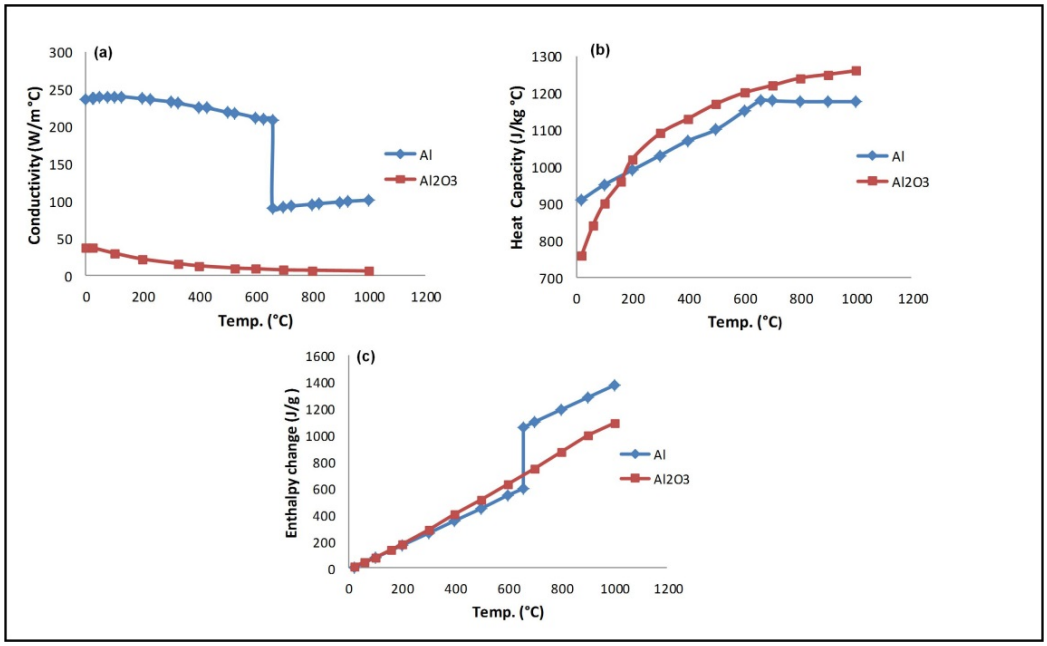

Figure 2. Thermophysical properties of Al and Al_2O_3 with temperature [20].

Within practical SLM applications, the volumetric energy density (ε) is used to systematically evaluate the influence of the process parameters that are employed; it can be expressed as [21]:

$$\varepsilon = \frac{P}{vhd} \qquad (7)$$

where *P* denotes the laser power, *v* and *h* represent the scanning speed and hatch spacing, respectively, and *d* is the powder layer thickness. An optimal volumetric energy density is required to produce high-quality component; finite element thermal analysis provides an effective and simple approach for predicting the optimal combination of process parameters.

Several existing studies(e.g. [8] [11] [13])have employed this basic heat-transfer model to investigate the thermal behaviour in SLM of metal powders such as stainless steel and titanium alloys and have proposed FEA techniques to simulate the addition of layers with time. Few studies

have concentrated on the thermal behaviour of aluminium alloy powder during SLM, however (one example is [12]), and none have focused on Al composites. In addition, certain limitations of previous work still exist that offer interesting directions for future studies. First, since the substrate is normally preheated to a specific temperature to avoid thermal distortion, the effect of temperature on absorptivity should thus be considered during SLM modelling and numerical simulation. Second, the high temperature that is produced at the laser-material interface may cause vaporisation, and the recoil pressure induced by vaporisation will give rise to spatter; thus, the potential vaporisation should be considered during the optimisation of process parameters.

To address this gap in the literature, this paper therefore investigates thermal behaviour during the scanning of the premier layer's Al-Al_2O_3 composite. The temperature dependent absorptivity was considered in the modelling, and the vaporisation that is induced by excessively high surface temperatures was considered when optimising the laser power and scanning speed. The consideration of the temperature-dependent absorptivity and vaporisation during the modelling and numerical simulation may thus be considered to be the main novelty of this work.

The Finite Element Model

This study used the ANSYS Multiphysics finite element package to build the premier layer's scanning model and to conduct the heat transfer numerical simulation used in the study. The 3D finite element model that was developed does not rely on 2D assumptions. Figure 3 shows the model and the scanning strategy in the premier layer. A rectangular composite powder layer of 5 x 1 x 0.05 mm was built on a 5 x 1 x 0.1 mm aluminium substrate. The nearly spherical ball-milled composite powder offered around 40% porosity, which was considered when defining the thermophysical properties during the modelling. The composite powder layer was meshed with 0.025 x 0.025 x 0.025 mm SOLID70 hexahedron element to improve calculation accuracy; coarse mesh was used for the substrate.

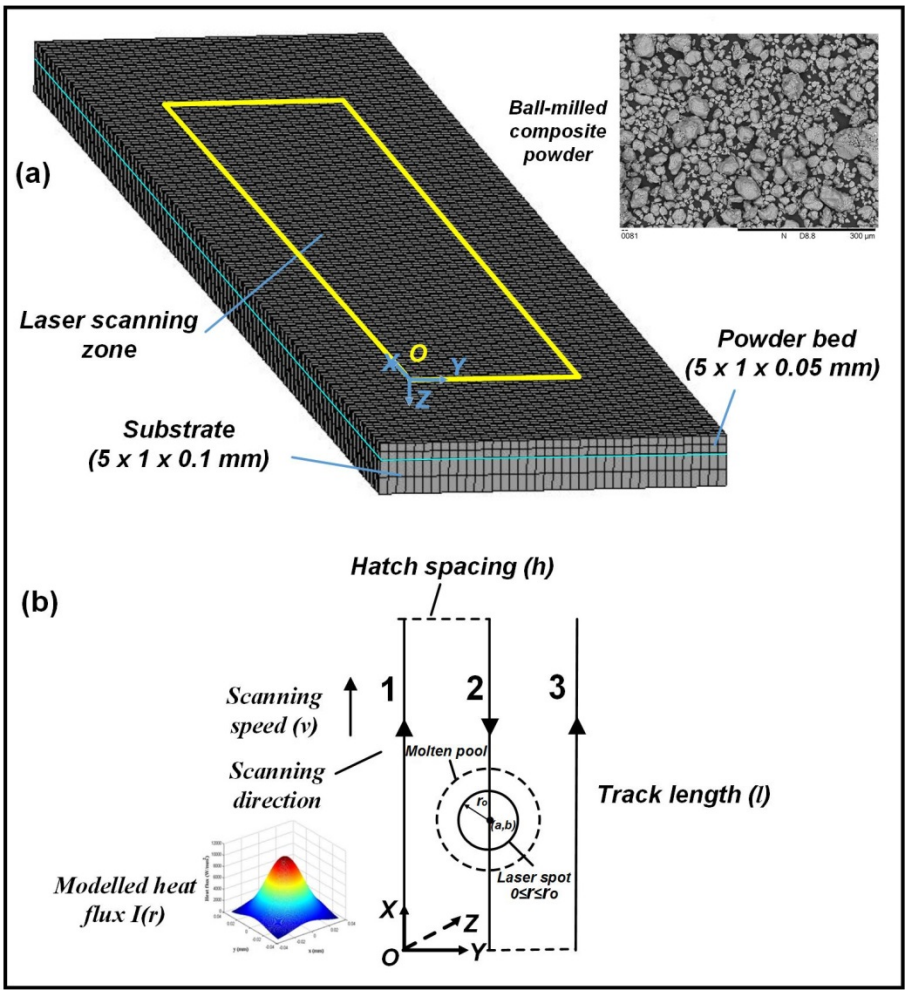

Figure 3. 3D finite element model and scanning strategy

In order to reduce the simulation time, the premier layer that was built was reduced to three scanning tracks; a bidirectional scanning strategy was employed to conduct the simulation. The heat flux *I(r)* followed a Gaussian distribution (Eq. [1]); the laser radial distance *r* can be expressed as:

$$r = \sqrt{(X-a)^2 + (Y-b)^2} \qquad (0 \le r \le r_0) \qquad (8)$$

where variables *a* and *b* can be determined as:

$$(a,b) = \begin{cases} (vt-(n-1)l,(n-1)h) & (n=1,3,5,\dots) \\ (nl-vt,(n-1)h) & (n=2,4,6,\dots) \end{cases} \qquad (9)$$

where v and t denote the scanning speed and scanning time, respectively; n and l represent track number and track length, respectively, and h is the hatch spacing. When three tracks are simulated, the variables a and b can then be determined as:

$$(a,b)=\begin{cases}(vt,0) & (0\le t\le \frac{l}{v})\\ (2l-vt,h) & (\frac{l}{v}<t\le \frac{2l}{v})\\ (vt-2l,2h) & (\frac{2l}{v}<t\le \frac{3l}{v})\end{cases} \quad (10)$$

In terms of Eq. (1), the heat-flux magnitude strongly depends on the laser power and powder absorptivity; Figure 4 shows the heat flux magnitude as a function of these two parameters. More specifically, when the absorptivity was fixed at 0.088 (at room temperature), the heat-flux magnitude was around 9 GW/m^2 when the laser power was relatively low, at 200 W; the heat-flux magnitude increased to 14 GW/m^2 when the laser power increased to 300 W; a 19 GW/m^2 heat-flux magnitude was reached when the laser power was increased to 400 W. Figure 4b shows the heat-flux magnitude increased from 14 GW/m^2 to 18 GW/m^2 when the powder absorptivity increased from 0.088 to 0.116. In general, a higher heat-flux magnitude leads to stronger laser energy and further generates higher temperatures at the laser-material interface.

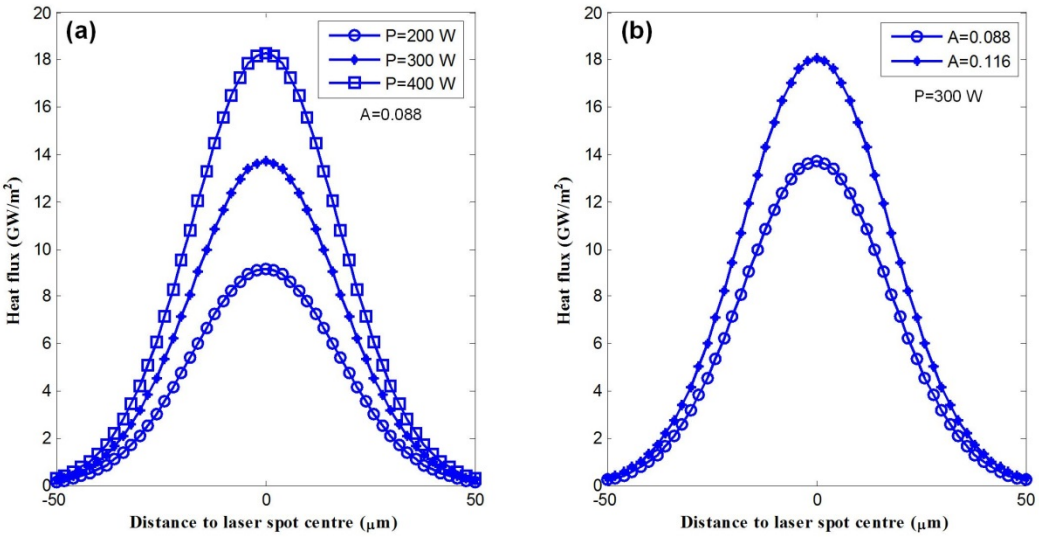

Figure 4. Heat-flux magnitude with laser power and absorptivity.

The following assumptions are made in this simulation in order to create a mathematically tractable model:

- The composite powder bed was assumed to be homogeneous and continuous.
- The heat flux from the laser beam was modelled as Gaussian-distributed heat flux and was given directly on the top of the composite powder bed.
- The laser spot was assumed to have a circular shape.
- The convective heat transfer coefficient between the environment and the powder bed was assumed to be a constant.
- Radiation was ignored.

Due to the laser scanning-induced temperature gradient in the powder bed, heat transfer occurred via convection between the powder bed and the ambient environment. The ambient temperature was maintained at 20°C; the convective heat transfer coefficient (*H*) can be expressed in *Z* direction, as follows:

$$-k_p \frac{\partial T}{\partial Z} = H(T_s - T_a) \qquad (11)$$

where k_p is thermal conductivity and T_s and T_a denote the powder bed surface temperature and ambient temperature, respectively. In general, *H* is set as 10 W/(m$^{2^\circ}$C) in finite element simulation [11]. Both the heat-flux and thermal-convection loads should be applied on the top surface of the composite powder layer; in order to prevent heat flux from overriding the applied convection load, it is necessary to create surface effect elements. Thermal convection was thus applied on the surface effect elements, and the heat flux was applied on the powder layer surface. The finite element simulation parameters that are chosen to simulate the scanning of the premier layer's composite powders are shown in Table 1.

Table 1. Finite element simulation parameters.

Parameters	**Value**	**Parameters**	**Value**
Absorptivity, *A*	11.6%	Convective heat transfer coefficient, *H*	10 W/(m^2°C)
Powder bed thickness, *d*	50 μm	Laser power, *P*	200, 300, 400 W
Laser spot radius, r_o	35 μm	Scanning speed, *v*	500, 1000,1250 and 1600 mm/s
Ambient temperature, T_a	20°C	Track length, *l*	4 mm
Number of tracks	3	Hatch spacing, *h*	100 and 150 μm

Results and Discussion

In order to fully melt an alumina particle, the maximum temperature induced by the laser radiation should be higher than the melting point of alumina (2040°C). Figure 5 shows the temperature variations of the midpoints in the three separate tracks under the following processing conditions: P=200 W, v=200 mm/s and h=100 μm. As the figure shows, the maximum temperature of the midpoints in the three tracks was more than 2200°C; track 2 and 3 demonstrated nearly the same maximum temperature, which was slightly higher than that of track 1. This can be attributed to the fact that the other two tracks would be pre-heated during the scanning of track 1. The simulation also showed a proper molten pool shape when the aforementioned process parameters were employed. In order to improve working efficiency within costly practical experiments, however, a higher laser power is generally preferred; the corresponding scanning speed and hatch-spacing parameters tend to increase in order to generate proper temperature distribution and molten pool during the SLM of Al-Al_2O_3 composite powder.

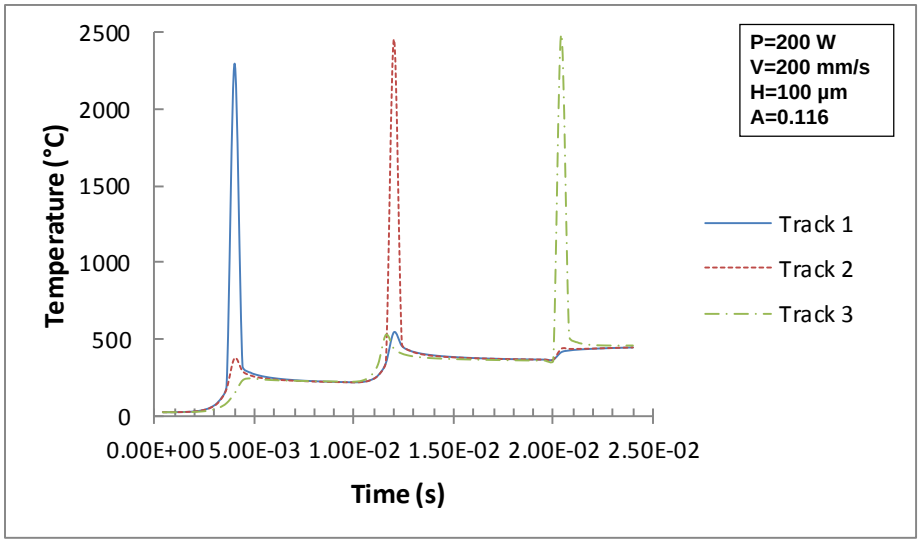

Figure 5. Temperature variations of the midpoints in three tracks with time.

Figure 6 shows the maximum temperature variations of the three separate tracks when different combinations of laser power and scanning speed were employed. More specifically, Figures 6a and b show the temperature variations when laser power was fixed at 300 W, while the scanning speed increased from 1000 mm/s to 1600 mm/s. It may be seen that the maximum temperature at the starting point of track 1 dropped from 3050°C to 2950°C with a 600 mm/s

increase in scanning speed. It is interesting to note that the maximum temperature increased dramatically at the beginning and kept steady afterwards, which could be explained by the fact that after roughly 1 mm length scanning, the solidification of the previous molten pool had finished due to the rapid cooling rate. The solidified metallic part exhibited much higher conductivity than the loose powder.

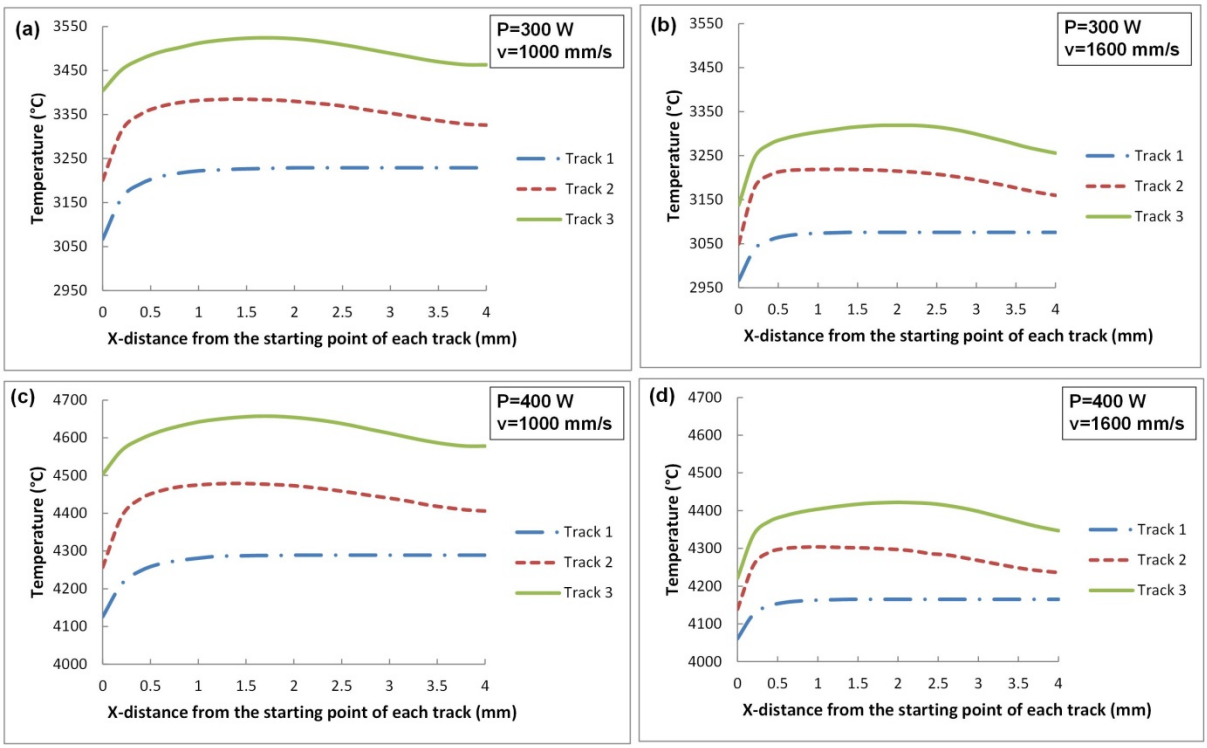

Figure 6. Maximum temperature variation of the three tracks.

A similar trend may also be observed at the beginning of track 2, but the maximum temperature decreased slightly until the end compared to the steady state in track 1; a 6°C temperature decrease was recorded between the peak and the end of track 2. This is perhaps because of the volume rise of the solidified part with the continued track scanning. Likewise, track 3 showed a similar temperature variation trend as track 2, but offered an average 150°C and 100°C higher than track 2 at each scanning point under the scanning speeds of 1000 mm/s and 1600 mm/s, respectively. It may be concluded that when laser power was fixed, a relatively higher scanning speed generated a lower maximum temperature during the SLM due to lower laser energy input.

Figures 6c and d, in contrast, show the results of employing a laser power of 400 W while scanning speeds are set at 1000 mm/s and 1600 mm/s, respectively. The maximum temperature

variation of the three tracks exhibited a trend similar to the variation observed when the laser power was 300 W. It should be noted, however, that the increased 100 W in laser power led to roughly 1000°C increase in temperature. The maximum temperatures in track 3 were 4657°C and 3522°C, as shown in Figures 6c and a, respectively, which indicates that when the scanning speed was fixed at 1000 mm/s, the increased laser power of 100 W led to a more than 1000°C temperature increase in the powder bed. The super high temperature tended to evaporate the liquid phase from the molten pool, however, and the recoil pressure induced by vaporisation could cause spatter and further decrease the layer thickness. It may also be concluded that the temperature generated was more sensitive to the laser power than to the scanning speed.

In order to further investigate the transient temperature distribution during the scanning of the premier layer, the temperature variation of the midpoint in track 2 was investigated during the scanning of the three tracks when different combinations of laser power and scanning speed were used (Figure 7).

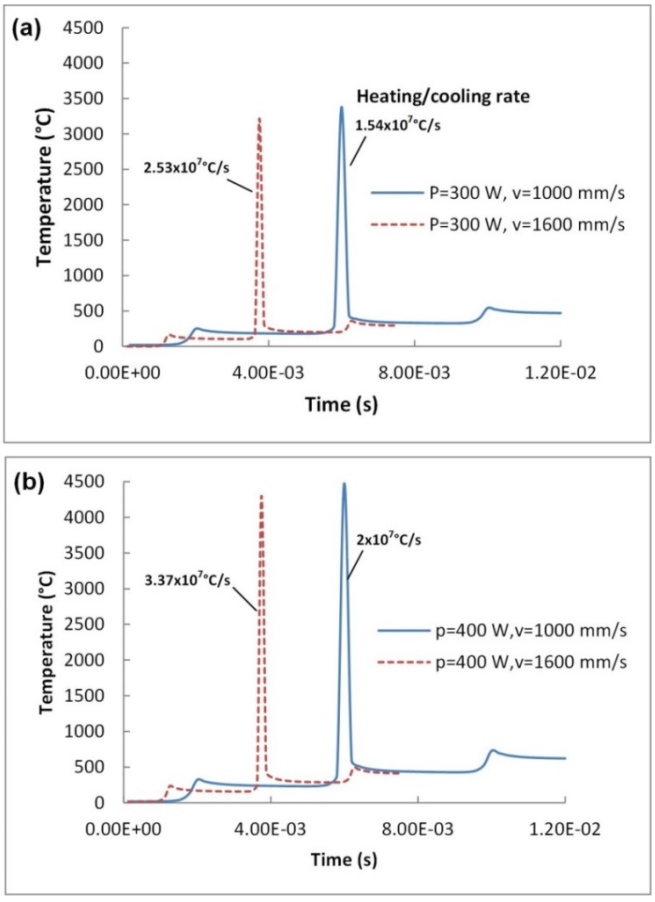

Figure 7. Temperature variation of the midpoint in track 2.

Figure 7a shows the temperature variation of the midpoint in track 2 when the laser power was fixed at 300 W. It may be seen that the temperature reached a peak of 3380°C at 0.006s when the scanning speed was at 1000 mm/s; a cooling rate of $1.54x10^{7}$°C/s could then be determined. Likewise, when the scanning speed increased to 1600 mm/s, the peak reached 0.00375s with the temperature of 3215°C; the calculated cooling rate was $2.53x10^{7}$ °C/s. It may be concluded that when the laser power was set at 300 W, the scanning speeds of both 1000 mm/s and 1600 mm/s could generate rapid cooling rates to produce very fine microstructures in the as-built parts. Figure 7b shows the temperature variation of the midpoint in track 2 when the laser power is fixed at 400 W and the determined peak temperature was 4473°C and 4299°C, respectively. Furthermore, the calculated cooling rate was $2x10^{7}$°C/s and $3.37x10^{7}$°C/s when the scanning speed was set at 1000 mm/s and 1600 mm/s, respectively.

It may be concluded that when the laser power was fixed, a lower maximum temperature and higher cooling rate could be generated with an increase in scanning speed. When the scanning speed was fixed, however, both the maximum temperature and the heating/cooling rate increased dramatically with an increase in laser power. The cooling rates are generally thought to be more sensitive to scanning speed rather than to laser power. In order to determine the laser power and scanning speed that are best suited for SLM of the composite powder, one should not only consider the maximum temperature and cooling rate but also take into account the molten pool dimensions. Figure 8a shows the molten pool temperature contours of the midpoint in track 2 when the laser power and scanning speed were set at 300 W and 1000 mm/s, from which three dimensions of the molten pool were measured from both the top surface and the cross-sectional profile. The predicted molten length was 165 μm compared to the width of 160 μm. It should be noted that the predicted molten pool width could guarantee an overlapping between two adjacent tracks; this overlapping further contributed to a strong bonding of the two rapidly solidified tracks. Under the process conditions, the predicted molten pool depth was 77 μm greater than the single powder layer thickness (50 μm) which implies that strong metallurgical bonding had occurred between the powder bed and the substrate.

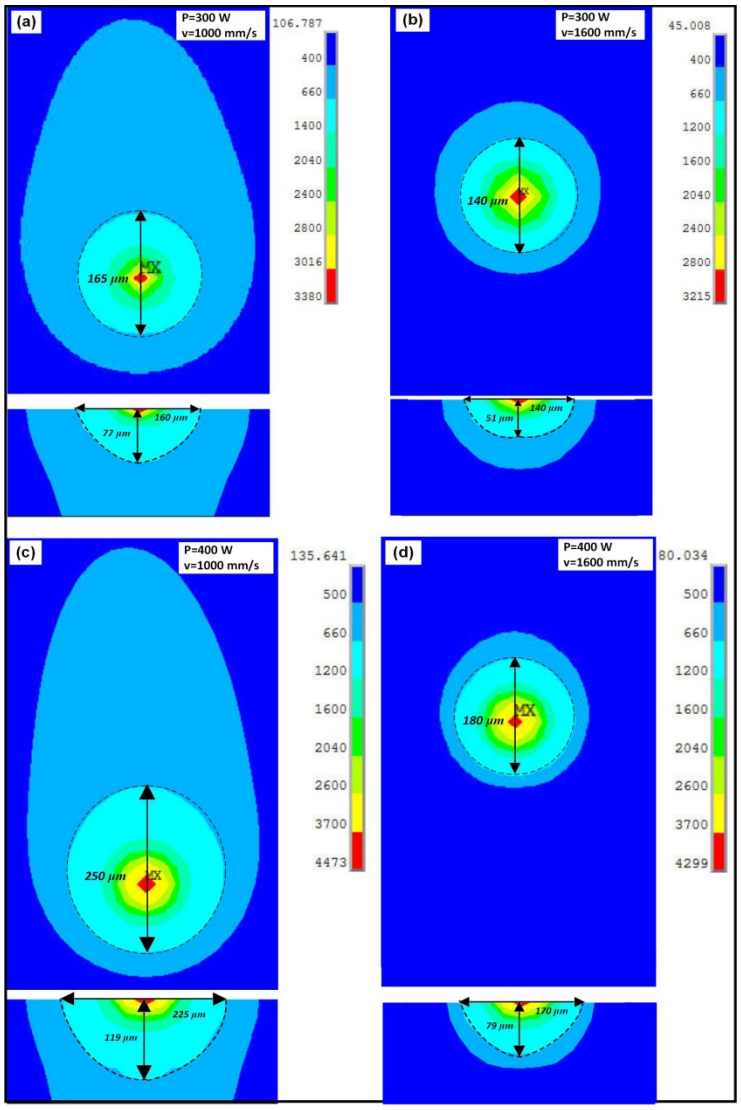

Figure 8. Molten pool dimensions of the midpoint in track 2 with laser power of 300W.

Figure 8b shows the predicted molten dimensions when the scanning speed increased to 1600 mm/s, from which the molten pool had the same measured length and width of 140 μm. The predicted pool depth was around 51 μm, which was very close to the single powder layer thickness; this situation implied poor metallurgical bonding between the powder bed and the substrate. It should be noted that poor metallurgical bonding leads to higher porosity levels whereas good bonding lead to minimum porosity. Our simulation results are thought to be consistent with the experimental results in [22], where the measured porosity increased from 0.7% to 2.3% when the scanning speed varied from 1000 mm/s to 1600 mm/s while maintaining laser power at 170 W. Qiu et al. [23] also determined similar findings (Figure 9a), from which the porosity of the as-built

Ti6Al4V specimens was relatively low when the scanning speeds were below 2700 mm/s; the measured porosity did increase with an increase in scanning speed, however (but below 4250 mm/s).

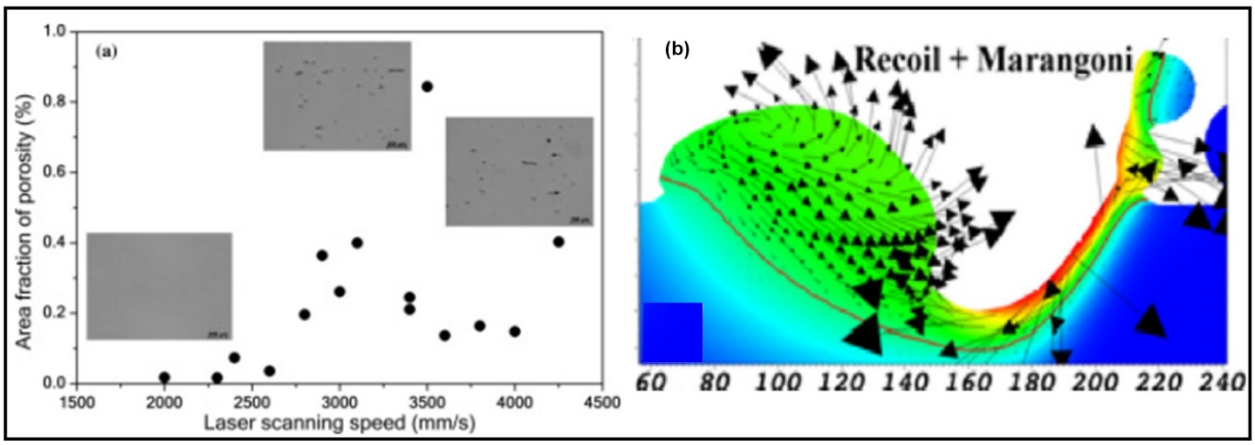

Figure 9. (a) Variation of porosity with laser power fixed at 400 W; (b) spatter and pores induced by recoil pressure and Marangoni [23] [24].

It should also be noted that the heat-affected zone (greater than 400°C) offered a significant difference in shape when the scanning speed increased from 1000 mm/s to 1600 mm/s. This can be explained by the fact that a lower scanning speed leads to a longer laser irradiation time, and the high temperature generated at the laser-material interface could be conducted to the rapidly solidified regions and produce a nearly elliptical heat-affected zone (Figure 8a). The predicted molten pool dimensions of the midpoint in track 2 are shown in Figures 8c and d when the laser power increased to 400 W. It may be seen that Figure 8c displays a similar heat-affected zone shape to Figure 8a, but it shows a much larger molten pool; this situation may be attributed this situation to higher laser energy input when a higher laser power was employed. Likewise, Figure 8d shows a similar heat-affected zone to Figure 8b, as well as a larger molten pool size. Furthermore, the situations shown in Figure 8c and d could guarantee strong bonding behaviours of the two adjacent tracks and two powder layers. It should be noted, however, that the generated maximum temperatures of 4473°C and 4299°C could evaporate the fluid out of the molten pool, thus resulting in porosity and spatter, both of which could contribute to poor mechanical properties of the as-built parts. This observation appears to be consistent with Khairallah et al.' findings [24] (Figure 9b), from which the recoil pressure induced by the vaporisation, together with the Marangoni convection, led to the spatter and depression of the molten pool. When the depression

collapsed, however, porosity could be formed in the as-built parts; the formed pores were detrimental to mechanical properties (e.g. yield strength, elongation).

Experimental work was conducted using the Renishaw AM250 in order to validate the simulation results. The laser power was maintained at 200 W while scanning speed varied between 200 mm/s and 600 mm/s (Figure 10). It can be seen that the measured melt pool with and depth decrease with an increase in scanning speed; the predicted melt pool depth decrease from 29 µm to 10 µm, which shows proper agreement with experimental results. It should be noted that, however, the track height that was produced using a layer thickness of 50 µm is less than the layer thickness and this might be attributed to the porosity of the powder bed and the spreading out of the melted metallic powder.

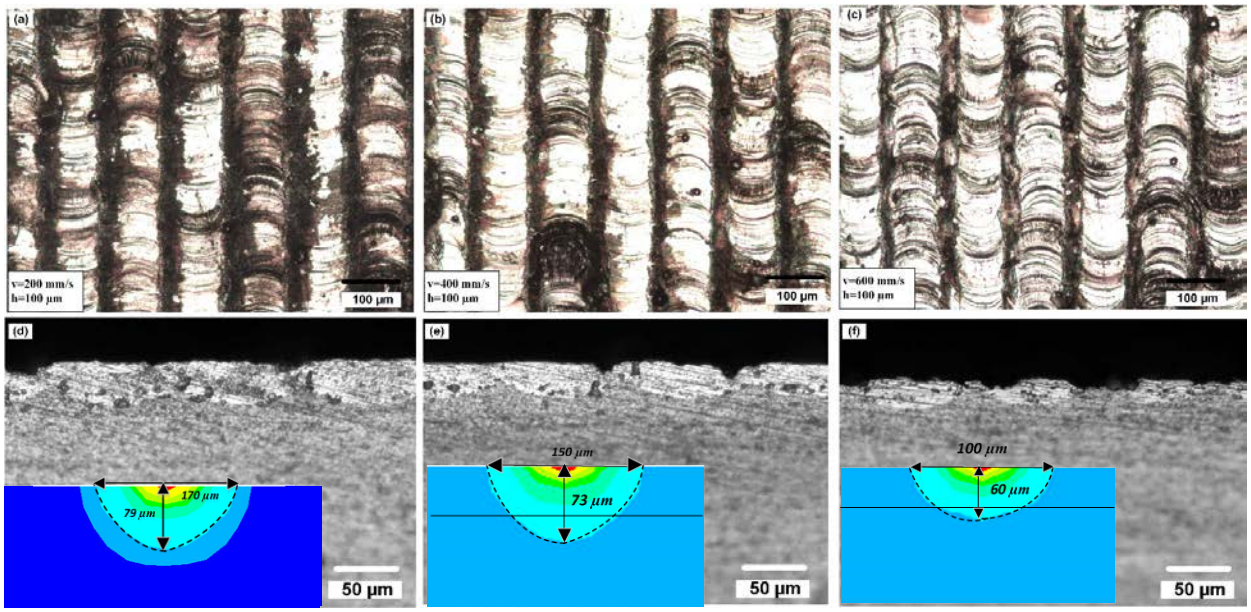

Figure 10. Experimental validation with laser power of 200 W

Conclusions

This study has developed a three-dimensional transient finite element model for predicting thermal behaviour during the scanning of the premier layer in SLM of Al-Al_2O_3 composite powders. The following conclusions have been drawn from the simulation results.

- The maximum temperature at each scanning point decreased with an increase in scanning speed and rose with an increase in laser power. Apart from the first scanned track, the

maximum temperature in the other tracks increased at the beginning and then decreased until the track scan was completed.

- The cooling rate was predicted to rise with an increase in both scanning speed and laser power, but it is thought to be more sensitive to scanning speed than to laser power. When laser power and scanning speed were fixed, however, the cooling rate that was determined remained constant; it was considered to be independent of the scanning positions. The dimensions of the molten pool are predicted to rise with an increase in laser power but decrease with an increase in scanning speed.
- When the laser power was set at 400 W, the predicted maximum temperature was above 4000°C when the scanning speeds employed were 1000 mm/s and 1600 mm/s. It is believed that he excessively high temperature resulted in vaporisation and other defects; in order to obtain high-quality parts, the recommended volumetric energy density is thus 40 J/mm^3 with laser power 300 W, scanning speed 1000 mm/s, hatch spacing 150 μm and layer thickness 50 μm. These findings will aid in developing an understanding of thermal behaviour during the SLM of AL-Al_2O_3 composites when optimising process parameters in order to produce high-quality parts with minimal defects and maximal efficiency.

References

[1] R. B. Patil and V. Yadava, "Finite element analysis of temperature distribution in single metallic powder layer during metal laser sintering," *Int. J. Mach. Tools Manuf.*, vol. 47, no. 7–8, pp. 1069–1080, 2007.

[2] S. Dadbakhsh and L. Hao, "Effect of Al alloys on selective laser melting behaviour and microstructure of in-situ formed particle reinforced composites," *J. Alloys Compd.*, vol. 541, pp. 328–334, 2012.

[3] L. Thijs, K. Kempen, J. P. Kruth, and J. Van Humbeeck, "Fine-structured aluminium products with controllable texture by selective laser melting of pre-alloyed AlSi10Mg powder," *Acta Mater.*, vol. 61, no. 5, pp. 1809–1819, 2013.

[4] M. Wong, S. Tsopanos, C. J. Sutcliffe, and I. Owen, "Selective laser melting of heat transfer devices," *Rapid Prototyp. J.*, vol. 13, no. 5, pp. 291–297, 2007.

[5] Q. Han, R. Setchi, and S. L. Evans, "Synthesis and characterisation of advanced ball-milled Al-Al2O3 nanocomposites for selective laser melting," *Powder Technol.*, vol. 297, pp. 183–192, 2016.

[6] P. Mercelis and J.-P. Kruth, “Residual stresses in selective laser sintering and selective laser melting,” *Rapid Prototyp. J.*, vol. 12, no. 5, pp. 254–265, 2006.

[7] T. H. C. Childs, C. Hauser, and M. Badrossamay, “Mapping and Modelling Single Scan Track Formation in Direct Metal Selective Laser Melting,” *CIRP Annals - Manufacturing Technology*, vol. 53, no. 1. pp. 191–194, 2004.

[8] T. Childs, “Selective laser sintering (melting) of stainless and tool steel powders: experiments and modelling,” *Proc. …*, vol. 219, no. 4, pp. 339–357, 2005.

[9] M. Matsumoto, M. Shiomi, K. Osakada, and F. Abe, “Finite element analysis of single layer forming on metallic powder bed in rapid prototyping by selective laser processing,” *Int. J. Mach. Tools Manuf.*, vol. 42, no. 1, pp. 61–67, 2002.

[10] K. Dai and L. Shaw, “Distortion minimization of laser-processed components through control of laser scanning patterns,” *Rapid Prototyping Journal*, vol. 8, no. 5. pp. 270–276, 2002.

[11] A. Hussein, L. Hao, C. Yan, and R. Everson, “Finite element simulation of the temperature and stress fields in single layers built without-support in selective laser melting,” *Mater. Des.*, vol. 52, pp. 638–647, 2013.

[12] Y. Li and D. Gu, “Parametric analysis of thermal behavior during selective laser melting additive manufacturing of aluminum alloy powder,” *Mater. Des.*, 2014.

[13] I. A. Roberts, C. J. Wang, R. Esterlein, M. Stanford, and D. J. Mynors, “A three-dimensional finite element analysis of the temperature field during laser melting of metal powders in additive layer manufacturing,” *Int. J. Mach. Tools Manuf.*, vol. 49, no. 12–13, pp. 916–923, 2009.

[14] Kolossov, E. Boillat, R. Glardon, P. Fischer, and M. Locher, “3D FE simulation for temperature evolution in the selective laser sintering process,” *Int. J. Mach. Tools Manuf.*, vol. 44, no. 2–3, pp. 117–123, 2004.

[15] N. K. Tolochko, Y. V. Khlopkov, S. E. Mozzharov, M. B. Ignatiev, T. Laoui, and V. I. Titov, “Absorptance of powder materials suitable for laser sintering,” *Rapid Prototyping Journal*, vol. 6, no. 3. pp. 155–161, 2000.

[16] W. Steen, K. Watkins, and J. Mazumder, *Laser matrial processing*. Springer Science & Business Media, 2010.

[17] N. T. Aboulkhair, N. M. Everitt, I. Ashcroft, and C. Tuck, “Reducing porosity in AlSi10Mg parts processed by selective laser melting,” *Addit. Manuf.*, vol. 1–4, pp. 77–86, 2014.

[18] L. Dong, a. Makradi, S. Ahzi, and Y. Remond, “Three-dimensional transient finite

element analysis of the selective laser sintering process," *J. Mater. Process. Technol.*, vol. 209, no. 2, pp. 700–706, 2009.

[19] F. Thummler and R. Oberacker, *An Introduction to Powder Technology*. London: The University Press, 1993.

[20] Hatch J.E., "Aluminum Properties and Physical Metallurgy," *ASM ,Ohio, US,* 1984.

[21] D. Gu, Y. C. Hagedorn, W. Meiners, K. Wissenbach, and R. Poprawe, "Nanocrystalline TiC reinforced Ti matrix bulk-form nanocomposites by Selective Laser Melting (SLM): Densification, growth mechanism and wear behavior," *Compos. Sci. Technol.*, vol. 71, pp. 1612–1620, 2011.

[22] K. Kempen, L. Thijs, E. Yasa, M. Badrossamay, W. Verheecke, and J. P. Kruth, "Process optimization and microstructural analysis for selective laser melting of AlSi10Mg," in *22nd Annual International Solid Freeform Fabrication Symposium - An Additive Manufacturing Conference, SFF 2011*, 2011, pp. 484–495.

[23] C. Qiu, C. Panwisawas, M. Ward, H. C. Basoalto, J. W. Brooks, and M. M. Attallah, "On the role of melt flow into the surface structure and porosity development during selective laser melting," *Acta Mater.*, vol. 96, pp. 72–79, 2015.

[24] S. A. Khairallah, A. T. Anderson, A. Rubenchik, and W. E. King, "Laser powder-bed fusion additive manufacturing: Physics of complex melt flow and formation mechanisms of pores, spatter, and denudation zones," *Acta Mater.*, vol. 108, pp. 36–45, 2016.